Kinetics of 1-Butyl and 2-Butyl Radical Reactions with Molecular Oxygen: Experiment and Theory

Arkke J. Eskola[1], Timo T. Pekkanen[1], Satya P. Joshi[1], Raimo S. Timonen[1], Stephen J. Klippenstein[2]*

[1] Molecular Science, Department of Chemistry, University of Helsinki, FI-00560 Helsinki, Finland

[2] Chemical Sciences and Engineering Division, Argonne National Laboratory, Argonne, IL 60439 USA

*Corresponding author's contact information:

Department of Chemistry, PO BOX 55 (A.I. Virtasen aukio 1), FIN-00014 University of Helsinki, Finland

Phone: +358 50 4489288

email: arkke.eskola@helsinki.fi

Colloquium: 1. Reaction Kinetics

Supplemental Material is available.

Total length of the paper determined with Method 1: 5825

Word equivalent length of main text: 3747; nomenclature: 0; references: 560; Fig 1. 269; Fig 2. 252; Fig 3. 252; Fig 4. 176; Fig 5. 287; Fig 6. 282

Abstract

The reaction of O_2 with butyl radicals is a key early step in the oxidation of butane, which is a prototypical alkane fuel with combustion properties that mimic those of many larger alkanes. Current combustion mechanisms employ kinetic descriptions for such radical oxidations that are based on fairly limited information. The present work employs a combination of experiment and theory to probe the kinetics of O_2 reacting with both *1*- and *2*-butyl radicals. The experiments employ laser photolysis to generate butyl radicals and thereby initiate the reaction kinetics. Photoionization mass spectrometric observations of the time-dependent butyl radical concentration yield rate constants for the overall reaction. The experiments cover temperatures ranging from 200 to 500 K and He bath gas pressures ranging from to 0.3 to 6 Torr. Ab initio transition state theory (TST) based master equation calculations are used to predict the kinetics over a broad range of conditions. The calculations consider both the barrierless R + O_2 entrance channel, treated with direct CASPT2 variable reaction coordinate TST, and the decomposition of the RO_2 complex to HO_2 + alkenes, treated with CCSD(T)/CBS based TST. Theory and experiment are in good agreement, with maximum discrepancies of about 30 %, suggesting the appropriateness of the theory based predictions for conditions of greater relevance to combustion. The kinetic description arising from this work should be of considerable utility to combustion modeling of butane, as well as of other related saturated hydrocarbons.

KEYWORDS: Radical reaction kinetics, photoionization mass spectrometer, 1-butyl and 2-butyl radicals, ab initio calculations, transition state theory, VRC-TST

1. Introduction

Reactions of alkyl radicals with molecular oxygen are ubiquitous in oxidative environments containing hydrocarbons; from atmospheric oxidation of anthropogenic and natural compounds to combustion of fuel – air mixtures to obtain power or thrust. In combustion environments, alkyl radicals are commonly formed through hydrogen atom abstraction reactions from paraffinic fuel molecules by atoms (H, $O(^3P)$) and other radicals (OH, HO_2, CH_3, etc.). At high temperatures, unimolecular decompositions of fuel molecules are also an important source of alkyl radicals.

The paraffinic content of transportation fuels is significant: gasoline largely originates (> 85 %) from saturated hydrocarbons, i.e., normal, branched, and cyclic paraffins. While jet and diesel fuels have a greater aromatic content, their paraffin content is still significant, mostly > 50 % [1,2]. Paraffinic hydrocarbons also comprise a significant fraction of surrogate fuels, whose purpose is to emulate highly complex real fuels [1,2]. Consequently, an accurate understanding of alkyl radical chemistry and kinetics under low, intermediate, and high temperature combustion conditions is crucial to reliable modelling of the combustion of almost any real or surrogate fuel.

A typical, detailed chemical kinetic model for combustion is nowadays composed of thousands of reactions; a recent *n*-butane oxidation model consists of 1328 reactions [3]. The kinetics and mechanism of any *single* reaction in these models may be based on estimates, on results of kinetic experiments [4,5], or, increasingly, on the predictions of computational reaction kinetics [6]. The reactions of alkyl radicals, R, with molecular oxygen, $R + O_2$ are often especially important reactions in combustion models. For example, the recent global sensitivity analysis of Hebrard et al. highlights the importance of this reaction for *n*-butane oxidation [7]; i.e., for the oxidation of n-butane in a jet stirred reactor the 1- and 2-butyl + O_2 addition reactions show up as the first and second most sensitive reactions, while the reactions to produce $C_4H_8 + O_2$ show up as the fifth or sixth most sensitive reactions for both autoignition delay times and oxidation in the jet stirred reactor.

Typically, an R + O_2 reaction may form stabilized RO_2 radical, directly form alkene + HO_2 radical products, or isomerize to a QOOH radical via internal H-atom abstractions. In turn, stabilized RO_2 may isomerize to QOOH under heated conditions and/or decompose back to reactants or on to alkene + HO_2 products. The QOOH may itself decompose to a cyclic ether + OH radical or again to alkene + HO_2 products [8,9]. Alternatively, the QOOH may react with a second O_2 molecule forming OOQOOH radical, which after internal H-atom abstraction and subsequent decomposition leads to labile ketohydroperoxide $HOOQ_{-H}$=O and OH radical [5,10]. This third reaction channel is particularly important because it leads to chain branching and ultimately ignition through the subsequent decomposition of the ketohydroperoxide to yield a total of 2 OH radicals + OQ_{-H}=O, that is three radicals [11,12]. This mechanism is especially important for paraffinic fuels.

The present study employs a combination of experiment and theory to probe the R + O_2 reaction kinetics for the two butyl radicals, 1- and 2- butyl, that arise via H abstractions from *n*-butane. The latter is a prototypical paraffinic fuel that exhibits combustion behavior representative of that found for the primary reference fuels *n*-heptane and *iso*-octane, as well as other saturated hydrocarbons. For example, it shows a classic negative temperature coefficient (NTC) regime [3,13] and the detailed molecular pathways are closely analogous to those expected to be most important for larger hydrocarbons [14,15]. Butyl radicals are also of interest because their molecular complexity provides a valuable tradeoff between experimental and theoretical concerns. In particular, the relatively small size of the butyl radical species facilitates high-level theoretical calculations. Nevertheless, it is large enough that there is substantial stabilization of the RO_2 species at pressures readily explored experimentally. As a result, accurate, direct time-resolved experiments can be conveniently performed with photoionization mass-spectrometry.

There exists only one previous direct kinetic study of 1-butyl and 2-butyl + O_2 reactions, which was performed at room temperature and 1 and 4 Torr pressure of helium buffer gas [16]. Lenhardt et al. [16] did not observe any pressure dependency for the kinetics of either reaction and suggested that their reported values are the high-pressure limiting values. The present experiments were performed

over a relatively large temperature range, 200 – 500 K, and over a moderate, but slightly larger, pressure range, 0.4 – 6 Torr. These new observations provide valuable further data regarding the temperature and pressure dependence of the kinetics, including the extent to which the observed rate coefficients are in their high-pressure limit, and, at higher temperatures, the effect of pressure on the stabilization rate.

The reaction of butyl radical with O_2 has been the subject of previous theoretical studies [8,14,15]. The early work of DeSain et al. [8] mapped the stationary points on the potential energy surface with a combination of QCISD(T) and MP2 ab initio and B3LYP density functional theory calculations. The most detailed prior theoretical study of butyl radical kinetics was provided by Miyoshi [15] who employed an ab initio TST based master equation approach [6,10] to treat the kinetics of the R + O_2 system for a range of radicals. Due to their interest in exploring a large number of systems, including radicals as large as iso-octyl, their analysis was based on limited CASPT2 (second order perturbation from a complete active space reference), B3LYP, and CBS-QB3 ab initio determinations. Furthermore, their TST analysis was based on traditional reaction path concepts, which are expected to be of limited accuracy for barrierless reactions due to the large amplitude coupled hindered rotor nature of the intermolecular motions in the transition state region. These limitations led them to implement empirical corrections to their PES in order to reproduce room temperature experimental observations, i.e., those of Lenhardt et al. [16] for 1 and 2-butyl.

Here, for the 1- and 2-butyl radicals, we proceed considerably beyond the wide-ranging analysis of Miyoshi with an implementation of the variable reaction coordinate (VRC)-TST approach [17] based on direct CASPT2 samplings [18] and with higher level ab initio evaluations of the stationary point properties. For simplicity, we focus our attention on the formation of the RO_2 complex from R + O_2 and its decay to HO_2 + alkene products. This focus allows for direct comparison with the present experimental observations. In doing so, we ignore the formation and decay of QOOH species, which, while important to the global kinetics, has little direct effect on the loss of radicals through the R + O_2 reaction.

The present experimental observations and theoretical analyses for the 1- and 2-butyl + O_2 reactions provide highly complementary information that result in a well-validated description of the kinetics. The experimental observations provide important constraints on key aspects of the theoretical analysis, such as the rates of collisional energy transfer. In turn, the theoretical analysis yields meaningful predictions for a very broad range of temperature and pressure. Notably, this study represents the first application of the direct CASPT2 VRC-TST methodology to fuels that demonstrate NTC behavior.

2. Experimental

In the experiments, butyl radicals were produced using excimer laser photolysis and photoionization mass-spectrometry (PIMS) was employed to follow their kinetics. Details of the experimental apparatus and procedures used have been described previously [19]. The gas mixture flowed through a tubular reactor containing radical precursor and O_2 in varying amounts, and helium carrier gas in large excess. The 1-butyl and 2-butyl radicals were produced from precursors at 193 or 248 nm by laser photolysis along the flow reactor. The 1-butyl radicals were generated at 193 nm either from 1-bromobutane or 2-hexanone, while the 2-butyl radicals were generated from 2-bromobutane at 248 nm. Alkyl bromides have been used extensively and successfully as photolytic sources of alkyl radicals in kinetic experiments of R + O_2 reactions due to their several desirable properties: fairly high vapor pressure and low melting point enabling measurements even at around 200 K as in this work, low reactivity of concomitantly formed bromine atom with alkyl bromide precursor (any chain-reaction from bromine atom + alkyl bromide reaction forming alkyl radical is very unlikely since the barrier for this reaction is much higher in energy than other channels), and a significant absorption cross-section extending down to 248 nm enabling production of radicals with little rovibrational excitation. 2-hexanone precursor was used to show that the results do not depend on the identity of the radical precursor (as may be seen from Table S1). Gas flow velocity through the temperature-controlled reactor was about 4 – 5 m s^{-1}, which ensured that the gas mixture was completely replaced between laser pulses with a repetition rate of 4 – 5 Hz. The combined maximum uncertainty in the stated temperature and uniformity of a temperature profile is about ± 5 K. Reactor tubes with different inner

diameters (8 – 17 mm), material (stainless steel, Pyrex), and coating (halocarbon wax, polydimethyl siloxane) were employed to cover experimental conditions. The microwave-powered resonance lamp was employed to selectively photoionize 1-butyl or 2-butyl radicals using a suitable combination of a salt window and Cl_2 gas in the lamp to produce radiation in the range 8.9 – 9.1 eV: for 1-butyl either a CaF_2 or a BaF_2 window was used, while for 2-butyl only BaF_2 was used. The ions formed were selected using a quadrupole mass-spectrometer based on their *m/z* ratio prior to their detection by an off-axis electron multiplier. The temporal ion count signal was amplified and collected using electronics and exponential function $[R]_t = exp(-k't) \times [R]_0$ was fitted to the data by the non-linear least-squares method. The collection continued until the 1-σ uncertainty in k', as returned by the fitting procedure, was considered acceptable, that is $\Delta k'/k' \leq 0.1$. A linear fit of these k'values versus $[O_2]$ returned bimolecular reaction rate coefficient with the 1-σ uncertainty typically less than 10 %. With an exception of 2-butyl + O_2 reaction measurements at $T \leq 243$ K where combination of relatively low sensitivity to detect 2-butyl radical and unusually challenging radical to produce especially at low temperatures caused higher than anticipated uncertainty, we estimate the overall uncertainty of the bimolecular reaction rate coefficient measurement is ± 25%.

3. Theory

3.1 Stationary Point Properties

The B2PLYP-D3/cc-pVTZ density functional method is used here to determine the rigid-rotor harmonic oscillator (RRHO) rovibrational properties for the relevant stationary points on the 1- and 2-butyl + O_2 potential energy surfaces. The M06-2X/cc-pVTZ density functional method is used to map out one-dimensional torsional potentials for each hindered rotor mode at each of the stationary points.

To obtain more accurate energies at these stationary point geometries we implement the CCSD(T)-F12b method for the cc-pVTZ-F12 and cc-pVQZ-F12 basis sets and employ a modest extrapolation to the complete basis set limit. As demonstrated in Ref. [20], various corrections (i.e., for higher order excitations, core-valence, relativistic, Born-Oppenheimer, and vibrational anharmonicity effects) can

have a significant effect on the predicted energies. For systems as large as $C_4H_9O_2$, such calculations are currently impractical. Instead, we presume here that the corrections are identical to those evaluated for the corresponding channels in the chemically similar $C_2H_5 + O_2$ system [6]; i.e., 0.18 and -0.52 kcal/mol for RO_2 and the HO_2 elimination TS, respectively, relative to $C_2H_5 + O_2$.

The predicted stationary point energies reported in Table S2 are very similar to earlier QCISD(T) based values [8]; differing by at most 0.8 kcal/mol. We expect that the present estimates have 2σ uncertainties of 0.4 kcal/mol or less. The greater binding energy for the 2-butyl case implies that it should be more readily stabilized. The significantly lower energy predicted for the elimination saddle point in the 2-butyl case has important ramifications for the collisionless limit of the kinetics. In contrast, at higher pressures the barriers relative to the wells are more relevant, and those barriers are quite similar for the 1 and 2-butyl cases, especially for the production of 1-C_4H_8.

The GAUSSIAN software package [21] was used to perform the DFT calculations, while MOLPRO [22] was used to perform the CCSD(T) and multireference calculations.

3.2 Barrierless Transition State

The VRC-TST approach, which includes a quantitative treatment of the full anharmonicity and mode coupling of the low frequency intermolecular motions, has previously been shown to provide accurate a priori rate predictions for a wide variety of radical-radical reactions [6,18]. High accuracy predictions with the VRC-TST method require accurate determinations of the intermolecular interaction energies for arbitrary orientations at separations spanning the transition state range. For butyl···O_2 this corresponds to C···O separations ranging from about 2 to 4 Å. Here, we implement a direct CASPT2/cc-pVDZ configurational sampling, which has proven to be an effective procedure for predicting the energies for this long-range weakly interacting region of space [18]. These calculations employ a 7-electron, 5-orbital (7e,5o) active space consisting of the (6e,4o) π space of O_2 together with the radical orbital for butyl.

Previously, we have refrained from applying the VRC-TST approach to radical + O_2 reactions because of a difficulty in obtaining low uncertainty estimates for these interaction energies. However, we have recently demonstrated that multireference based evaluations (e.g., CASPT2 or multireference configuration interaction (MRCI)) of the splitting between high and low spin states, coupled with CCSD(T) based evaluations of the high spin interaction energies, yields what appear to be reliable interaction energies for this class of reactions [23]. This discovery provided the basis for the recent direct CASPT2 based VRC-TST studies of the C_2H_5, C_2H_3, and aromatic radical + O_2 reactions [6,23,24]. Here, this spin-splitting method is used to evaluate the energies along an approximate minimum energy path (cf. Fig. S1 and S2), which are then used to define a one-dimensional (R_{CO} dependent) correction to the reference CASPT2(7e,5o)/cc-pVDZ energies.

Corrections for geometry relaxation effects are commonly included in VRC-TST calculations. They are particularly important for radical + O_2 reactions due to the relatively gradual formation of the chemical bond arising from the need to first break the resonance stabilization of O_2. Notably, this geometry relaxation correction is sensitive to the OOCC torsional angle (cf. Figs. S3 and S4). Thus, this correction was evaluated as a function of both R_{CO} and the OOCC torsional angle through CASPT2(7e,5o)/aug-cc-pVDZ evaluations of the distinguished coordinate MEP with and without constraints on the fragment structures.

The VaReCoF software [25] was used to perform these VRC-TST calculations. Further details of these VRC-TST calculations are provided in the Supplemental Material.

3.3 Pressure Dependent Kinetics

Predictions for the temperature and pressure dependent phenomenological rate coefficients for the addition, and the direct and indirect HO_2 eliminations on the 1- and 2-butyl + O_2 PESs were obtained with the ab initio TST based ME approach [6,26]. The flux for the R + O_2 channel was evaluated with VRC-TST as described above, while conventional TST was used for the elimination channels with

RRHO assumptions for all but the torsional modes. The torsional modes were treated as 1-dimensional hindered rotors. Eckart based tunneling corrections were included for the elimination channels.

The collisional energy transfer rates were approximated as the product of Lennard-Jones collision rates with the exponential down model for the transition probability. The Lennard Jones σ and ε parameters were set to 2.55 Å and 7.1 cm^{-1}, 3.79 Å and 50 cm^{-1}, and 5.2 Å and 361 cm^{-1} for He, N_2, and $C_4H_9O_2$, respectively [15,27]. For He, the average downwards energy transferred, $<\Delta E_d>$, was set to 300 $(T/300)^{0.85}$ cm^{-1}, with the prefactor in this expression obtained from a fit to the experimental data. For N_2, $<\Delta E_d>$ was set to 390 $(T/300)^{0.75}$ cm^{-1}, with the increase in the prefactor and the decrease in the exponent based on qualitative consideration of the extensive energy transfer data reported by Jasper et al. [28].

The master equation calculations were performed with the MESS software [29,30].

4. Results and Discussion

In a set of experiments to measure the bimolecular rate coefficients for the 1- and 2-C_4H_9 + O_2 reactions, the radical R ion signal profile was first monitored in the absence of added molecular reactant O_2 to measure the ”wall reaction” rate, k_{wall}. The radical concentration after photolysis was kept low, below about 2×10^{11} cm^{-3}, to effectively suppress radical–radical reactions. The first order decay rate k_{wall} consists of all first order processes occurring in the reaction mixture and on the reactor wall without added O_2 reactant. The first order decay rate k' of the radical R signal was next measured as a function of added O_2 concentration under pseudo-first-order conditions. Since the only significant reactions consuming R during these experiments were the R + O_2 and wall reactions, the bimolecular reaction rate coefficient k(R + O_2) could be obtained from the slope of a line fitted through these decay rates k' when plotted versus [O_2]: under these experimental conditions $k'(\mathrm{R}+\mathrm{O}_2) = k(\mathrm{R}+\mathrm{O}_2) \times [\mathrm{O}_2] + k_{wall}$. Figure 1 shows a plot of the first order 1-C_4H_9 decay rate $k'(1\text{-}\mathrm{C}_4\mathrm{H}_9+\mathrm{O}_2)$ vs. [O_2] at T = 221 K and P = 0.86 Torr from which the bimolecular rate coefficient for the 1-C_4H_9 + O_2 reaction,

$k(1\text{-}C_4H_9+O_2)$, under these conditions is obtained. In Fig. 1 two examples of 1-C_4H_9 radical decays are also shown.

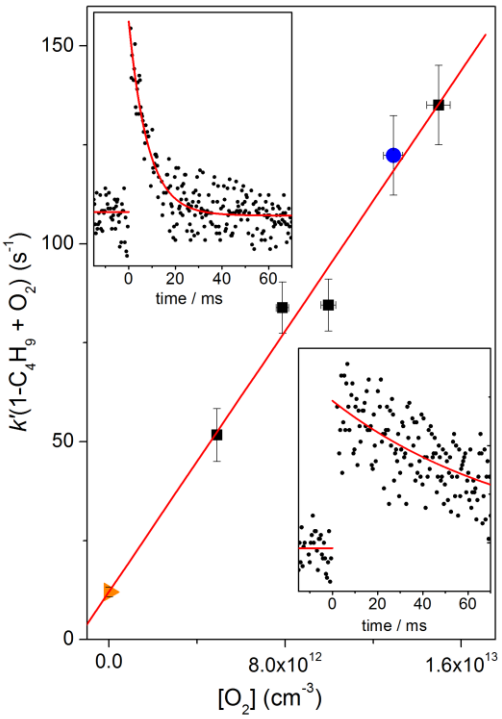

Figure 1. Plot of the first order 1-C_4H_9 decay rate coefficient k' *versus* [O_2] at T = 221 K at about 0.86 Torr pressure employing the 17 mm i.d. reactor tube (see table S1). Insets show actual ion signal profiles for the 1-C_4H_9 decays in the absence of the O_2-reactant (right) and in the presence of the [O_2] = 1.29×10^{13} cm^{-3} (left). Corresponding decay rates are k_{wall} = 12 ± 1.2 s^{-1} and k' = 122 ± 10 s^{-1} and are shown as solid orange triangle and solid blue circle in the plot, respectively. Uncertainties are one-standard deviation (1σ).

Kinetic experiments to determine bimolecular rate coefficients for the 1-C_4H_9 + O_2 and 2-C_4H_9 + O_2 reactions were performed over temperature (200 – 500 K) and total density ($0.9 – 15\times10^{16}$ cm^{-3}) ranges using helium buffer gas ([He]/[total] > 99 %). The results and conditions of the kinetic experiments for 1-C_4H_9 + O_2 and 2-C_4H_9 + O_2 reactions are shown in tables S1 and S3, respectively. These measurements are compared with the corresponding theoretical predictions in Figs. 2 and 3. The current experimental bimolecular rate coefficients for 1-butyl and 2-butyl + O_2 reactions agree with the results of Lenhardt et al. to within the stated uncertainties under corresponding conditions.

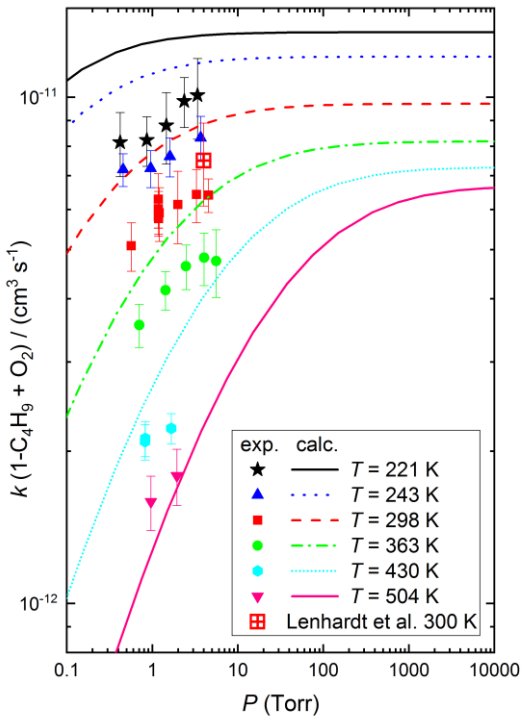

Figure 2. Plot of the experimentally observed (symbols) and theoretically predicted (lines) bimolecular rate coefficients for the 1-butyl + O_2 reaction.

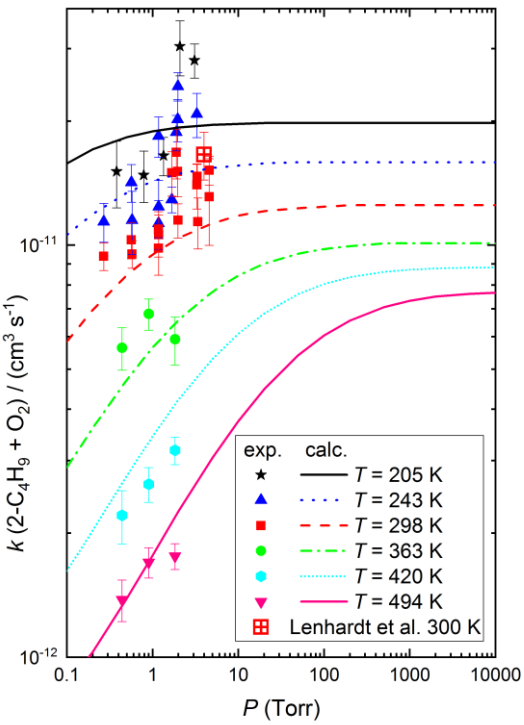

Figure 3. Plot of the experimentally observed (symbols) and theoretically predicted (lines) bimolecular rate coefficients for the 2-butyl + O_2 reaction.

For both reactions, there is good agreement between theory and experiment, with maximum discrepancies of about 20% for 2-butyl and about 40% for 1-butyl. Such discrepancies are within the expected accuracy of the theoretical calculations given the difficulty of treating O_2 reactions with VRC-TST. For 1-butyl, simply reducing the high pressure recombination rate by a factor of 0.7 yields predictions that smoothly interpolate the experimental data for all but the highest temperature. Meanwhile, the plot in Fig. S6 demonstrates that just reducing it by the more modest factor of 0.8 brings theory and experiment into agreement to within the latter's error bars.

Notably, at the highest temperatures, the experimental observations are quite far from the high-pressure limit. This data provides strong constraints for the stabilization part of the theoretical model and particularly the average downwards energy transfer parameter. Meanwhile, at the lowest temperature the experiments are very close to the high-pressure limit and the data provides strong constraints for the capture part of the theoretical model.

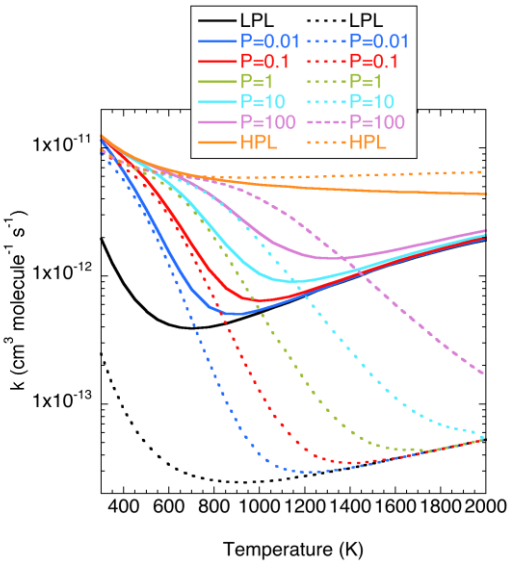

Figure 4. Plot of the theoretically predicted temperature and pressure dependence of the bimolecular rate coefficient for 1-butyl + O_2 (dashed) and 2-butyl + O_2 (solid) reactions. LPL and HPL denote collisionless and high-pressure limits, respectively, while the numerical values denote pressures in bar.

The theoretical model has been used to predict the rate coefficients for the R + O_2 system over a broad range of temperature and pressure (cf. Fig. 4 and supplemental material). At low pressures,

and/or at high temperatures, the total bimolecular rate coefficient becomes pressure independent, with the reaction producing HO_2 + alkenes. The presence of an additional HO_2 elimination channel and the lower barrier heights relative to the entrance channel lead to an order magnitude larger collisionless limit rate coefficient for the 2-butyl + O_2 reaction.

Modified Arrhenius representations of the theoretical predictions for the $C_4H_9 + O_2 \rightarrow C_4H_9O_2$, $C_4H_9 + O_2 \rightarrow C_4H_8 + HO_2$, and $C_4H_9O_2 \rightarrow C_4H_8 + HO_2$ rate coefficients are provided in Table S4 for a range of pressures for both 1-butyl and 2-butyl. These fits are based on calculation for N_2 as the collider, and employ the ad hoc factor of 0.8 reduction in the high-pressure limit for the 1-butyl + O_2 reaction.

In Fig. 5 different expressions for the temperature and pressure dependency of the bimolecular rate coefficients for the 1-$C_4H_9 + O_2 \rightarrow$ 1-C_4H_9OO and 2-$C_4H_9 + O_2 \rightarrow$ 2-C_4H_9OO reactions are compared. For 1-$C_4H_9 + O_2 \rightarrow$ 1-C_4H_9OO the current results indicate a faster reaction than previous studies, especially at 10 bar pressure, where the bimolecular rate coefficients from this study in the 700 – 1100 K temperature range are up to five times larger than the previous values of Hebrard [7], used in combustion kinetic models. Agreement between the current and previous studies is better for the 2-$C_4H_9 + O_2 \rightarrow$ 2-C_4H_9OO reaction with the current results a maximum of 2.5 times larger than previous predictions.

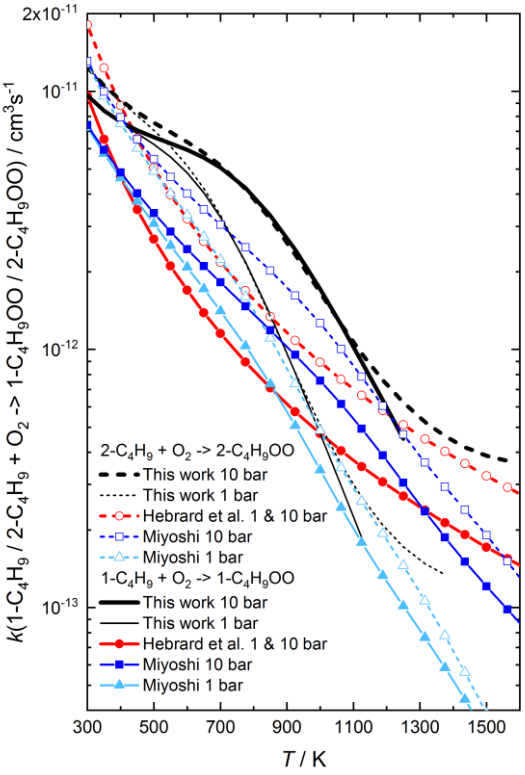

Figure 5. Plot of various predictions for the temperature dependence of the bimolecular rate coefficients for 1-C_4H_9 + O_2 → 1-C_4H_9OO and 2-C_4H_9 + O_2 → 2-C_4H_9OO at 1 and 10 bar. Results from the present work are compared with expressions from the literature [7,15].

In Fig. 6, the present predictions for the temperature dependence of the bimolecular rate coefficients for 1-C_4H_9 + O_2 → 1-C_4H_8 + HO_2 and 2-C_4H_9 + O_2 → 1-C_4H_8 / 2-C_4H_8 + HO_2 reactions are compared with those from Hebrard [7]. For 1-C_4H_9 the two predictions differ by more than an order of magnitude at all temperatures. Meanwhile, for 2-C_4H_9 the predictions are roughly equivalent at high temperature, but increasingly diverge as the temperature decreases below 900 K.

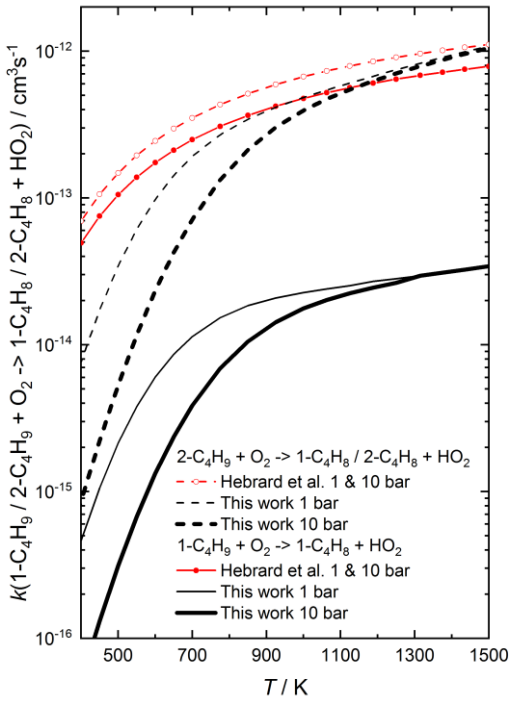

Figure 6: Plot of various predictions for the temperature dependence of the bimolecular rate coefficients for 1-C_4H_9 + O_2 → 1-C_4H_8 + HO_2 and 2-C_4H_9 + O_2 → 1-C_4H_8 / 2-C_4H_8 + HO_2 at 1 and 10 bar. Results from the present work are compared with the expressions from Hebrard [7].

The sensitivity of the present rate predictions to the energy transfer parameters, barrier height, and well depth are explored in the Supplemental Material (Figs. S6 to S10). The observed sensitivities, together with the good agreement observed between theory and experiment suggest that the present predictions are accurate to within a factor of 1.5 to 2.

5. Conclusions

Direct, time-resolved measurements of the decay of photolysis induced butyl radical signals have been used to observe the bimolecular rate coefficients for 1- and 2-butyl reacting with O_2 over the 200 – 500 K temperature range and pressures of 0.4 – 6 Torr. Related ab initio TST based master equation predictions provide a fairly accurate reproduction of the experimental observations. The low temperature experimental observations validate the VRC-TST based calculation of the capture rate, while the higher temperature measurements validate the underlying treatment of the pressure dependence. The good agreement between theory and experiment lends confidence to the kinetic

predictions obtained from application of the theoretical model over a broader range of conditions. The modified Arrhenius representations of these data are expected to find utility in combustion models for alkyl radical oxidation.

Acknowledgements

A. J. E. and S. P. J. acknowledge support from the Academy of Finland, Grant numbers 288377 and 294042. T. T. P. acknowledges support from the Doctoral Programme in Chemistry and Molecular Sciences of the University of Helsinki. Part of this material is based on work at Argonne supported by the U.S. Department of Energy, Office of Basic Energy Sciences, Division of Chemical Sciences, Geosciences, and Biosciences, under Contract No. DE-AC02-06CH11357 as part of the Argonne-Sandia Consortium on High-Pressure Combustion Chemistry, (ANL FWP # 59044).

Separate List of Figure Captions

Figure 1. Plot of first order 1-C_4H_9 decay rate coefficient k' *versus* [O_2] at T = 221 K at about 0.86 Torr pressure employing the 17 mm i.d. reactor tube (see table S1). Insets show actual ion signal profiles for the 1-C_4H_9 decays in the absence of the O_2-reactant (right) and in the presence of the [O_2] = 1.29×10^{13} cm^{-3} (left). Corresponding decay rates are k_{wall} = 12 ± 1.2 s^{-1} and k' = 122 ± 10 s^{-1} and are shown as solid orange triangle and solid blue circle in the plot, respectively. Uncertainties are one-standard deviation (1σ).

Figure 2. Plot of the experimentally observed (symbols) and theoretically predicted (lines) bimolecular rate coefficients for the 1-butyl + O_2 reaction.

Figure 3. Plot of the experimentally observed (symbols) and theoretically predicted (lines) bimolecular rate coefficients for the 2-butyl + O_2 reaction.

Figure 4. Plot of the theoretically predicted temperature and pressure dependence of the bimolecular rate coefficient for 1-butyl + O_2 (dashed) and 2-butyl + O_2 (solid) reactions. LPL and HPL denote collisionless and high-pressure limits, respectively, while the numerical values denote pressures in bar.

Figure 5. Plot of various predictions for the temperature dependence of the bimolecular rate coefficients for 1-C_4H_9 + O_2 → 1-C_4H_9OO and 2-C_4H_9 + O_2 → 2-C_4H_9OO at 1 and 10 bar. Results from the present work are compared with expressions from the literature [7,15].

Figure 6: Plot of various predictions for the temperature dependence of the bimolecular rate coefficients for 1-C_4H_9 + O_2 → 1-C_4H_8 + HO_2 and 2-C_4H_9 + O_2 → 1-C_4H_8 / 2-C_4H_8 + HO_2 at 1 and 10 bar. Results from the present work are compared with the expressions from Hebrard [7].

Supplemental Material (SM), content, and list of captions

File name: SM for Kinetics of 1-Butyl and 2-Butyl Radical Reactions with Molecular Oxygen: Experiment and Theory (Proc. Combust. Inst. 37, 2019).docx; Contains tables of measured bimolecular reaction rate coefficients, further details of the theoretical analysis, and modified Arrhenius representations of the theoretical rate predictions, all of which support the conclusions from this work.

Fig. S1. Plot of the CASPT2 (RS2C), IPEA shifted CASPT2 (RS2C;ipea), and MRCI+Q (CI+QC) predictions of the 1-butyl + O_2 interaction energies along an approximate MEP. The dashed lines denote the direct calculations of the doublet state interaction energies, while the solid lines denote their derivation from the spin-splitting approach.

Fig. S2. Plot of the CASPT2 (RS2C), ipea shifted CASPT2 (RS2C;ipea), and MRCI+Q (CI+QC) predictions of the 2-butyl + O_2 interaction energies along an approximate MEP. The dashed lines denote the direct calculations of the doublet state interaction energies, while the solid lines denote their derivation from the spin-splitting approach.

Fig. S3. Plot of the CASPT2/aug-cc-pVDZ evaluated geometry relaxation correction along the R_{CO} distinguished coordinate MEP for 1-butyl + O_2. The numerical values in the label denote different values of the OOCC torsional angle.

Fig. S4. Plot of the CASPT2/aug-cc-pVDZ evaluated geometry relaxation correction along the R_{CO} distinguished coordinate MEP for 2-butyl + O_2. The numerical values in the label denote different values of the OOCC torsional angle.

Fig. S5. Plot of the distinguished coordinate (R_{CO}) MEPs for O_2 adding to 1- and 2-butyl radicals.

Fig. S6. Plot of the experimentally observed (symbols) and theoretically predicted (lines) bimolecular rate coefficients for the 1-butyl + O_2 reaction. The theoretical predictions employ different values for the parameter denoting the average downwards energy transferred at room temperature. The solid lines employ the reference value of 300 cm^{-1}, while the dotted and dashed lines employ values of 200 and 450 cm^{-1}, respectively.

Fig. S7. Plot of the experimentally observed (symbols) and theoretically predicted (lines) bimolecular rate coefficients for the 2-butyl + O_2 reaction. The theoretical predictions employ different values for the parameter denoting the average downwards energy transferred at room temperature. The solid lines employ the reference value of 300 cm^{-1}, while the dotted and dashed lines employ values of 200 and 450 cm^{-1}, respectively.

Fig. S8. Plot of the experimentally observed (symbols) and theoretically predicted (lines) bimolecular rate coefficients for the 1-butyl + O_2 reaction. The theoretical predictions employ different values for the 1-$C_4H_9O_2$ well depth. The solid lines employ the reference values, while the dotted and dashed lines employ values shifted up and down by 0.4 kcal/mol, respectively.

Fig. S9. Plot of the experimentally observed (symbols) and theoretically predicted (lines) bimolecular rate coefficients for the 2-butyl + O_2 reaction. The theoretical predictions employ different values for the 2-$C_4H_9O_2$ well depth. The solid lines employ the reference values, while the dotted and dashed lines employ values shifted up and down by 0.4 kcal/mol, respectively.

Fig. S10. Plot of the theoretically predicted collisionless limit rate coefficients for the 1-butyl + O_2 and 2-butyl + O_2 reactions. The theoretical predictions employ either the reference barrier heights (solid lines) for the transiton states producing C_4H_8 + HO_2 or values shifted up (dashed) or down (dotted) by 0.4 kcal/mol.

Table S1. Conditions and results of the experiments used to measure the bimolecular rate coefficients of *n*-C_4H_9 + O_2 reaction. The shown error limits in k_w are 1σ fitting uncertainties only, while error limits in bimolecular reaction rate coefficients k are 1σ fitting uncertainties + estimate of other uncertainties.

Table S2. Stationary point energies for the 1- and 2-butyl + O_2 reactions.

Table S3. Conditions and results of the experiments used to measure the bimolecular rate coefficients of *s*-C_4H_9 + O_2 reaction. The shown error limits in k_w are 1σ fitting uncertainties only, while error limits in bimolecular reaction rate coefficients k are 1σ fitting uncertainties + estimate of other uncertainties.

Table S4. Modified Arrhenius representations of the rate coefficients for the 1- and 2-butyl + O_2 reaction systems (in ChemKin PLOG format).

References

[1] H.R. Zhang, E.G. Eddings, A.F. Sarofim, C.L. Mayne, Z. Yang, R.J. Pugmire, Selection of surrogates for jet fuels, in: H. Bockhorn, A. D'Anna, A.F. Sarofim, H. Wang (Eds.) Combustion Generated Fine Carbonaceous Particles, KIT Scientific Publishing, 2009, pp. 137 - 161.
[2] C.J. Mueller, W.J. Cannella, J.T. Bays, T.J. Bruno, K. DeFabio, H.D. Dettman, R.M. Gieleciak, M.L. Huber, C.B. Kweon, S.S. McConnell, W.J. Pitz, M.A. Ratcliff, Energy & Fuels, 30 (2016) 1445-1461.
[3] D. Healy, N.S. Donato, C.J. Aul, E.L. Petersen, C.M. Zinner, G. Bourque, H.J. Curran, Combust. Flame, 157 (2010) 1526-1539.
[4] J.D. DeSain, S.J. Klippenstein, J.A. Miller, C.A. Taatjes, J. Phys. Chem. A, 107 (2003) 4415-4427.
[5] A.J. Eskola, O. Welz, J. Zador, I.O. Antonov, L. Sheps, J.D. Savee, D.L. Osborn, C.A. Taatjes, Proc. Combust. Inst., 35 (2015) 291-298.
[6] S.J. Klippenstein, Proc. Combust. Inst., 36 (2017) 77-111.
[7] E. Hebrard, A. S. Tomlin, R. Bounaceur, F. Battin-Leclerc, Proc. Combust. Inst. 35 (2015) 607-616.
[8] J.D. DeSain, C.A. Taatjes, J.A. Miller, S.J. Klippenstein, D.K. Hahn, Faraday Discuss. 119 (2001) 101-120.
[9] A.J. Eskola, O. Welz, J.D. Savee, D.L. Osborn, C.A. Taatjes, J. Phys. Chem. A, 117 (2013) 12216-12235.
[10] C.F. Goldsmith, W.H. Green, S.J. Klippenstein, J. Phys. Chem. A, 116 (2012) 3325-3346.
[11] C.F. Goldsmith, M.P. Burke, Y. Georgievskii, S.J. Klippenstein, Proc. Combust. Inst., 35 (2015) 283-290.
[12] S.S. Merchant, C.F. Goldsmith, A.G. Vandeputte, M.P. Burke, S.J. Klippenstein, W.H. Green, Combust. Flame 162 (2015) 3658-3673.
[13] M. Cord, B. Sirjean, R. Fournet, A. Tomlin, M. Ruiz-Lopez, F. Battin-Leclerc, J. Phys. Chem. A 116 (2012) 6142-6158.
[14] S.M. Villano, L.K. Huynh, HH Carstensen, A.M. Dean, J. Phys. Chem. A 115 (2011) 13425-13442.
[15] A. Miyoshi, Int. J. Chem. Kinet. 44 (2012) 59-74.
[16] T.M. Lenhardt, C.E. McDade, K.D. Bayes, J. Chem. Phys., 72 (1980) 304-310.
[17] S.J. Klippenstein, J. Chem. Phys. 96 (1992) 367-371.
[18] S.J. Klippenstien, Y. Georgievskii, L.B. Harding, Phys. Chem. Chem. Phys. 8 (2006) 1133-1147.
[19] A.J. Eskola, R.S. Timonen, Phys. Chem. Chem. Phys., 5 (2003) 2557-2561.
[20] S.J. Klippenstein, L.B. Harding, B. Ruscic, J. Phys. Chem. A 121 (2017) 6580-6602.
[21] M. J. Frisch, G. W. Trucks, H. B. Schlegel, G. E. Scuseria, M. A. Robb, J. R. Cheeseman, G. Scalmani, V. Barone, B.; Mennucci, G. A. Petersson, et al. Gaussian 09, Revision D.1; Gaussian, Inc.: Wallingford, CT, 2009.
[22] MOLPRO, version 2015.1, a package of ab initio programs, H.-J. Werner, P. J. Knowles, G. Knizia, F. R. Manby, M. Schutz, and others, see http://www.molpro.net
[23] C.F. Goldsmith, L.B. Harding, Y. Georgievskii, J.A. Miller, S.J. Klippenstein, J. Phys. Chem. A, 119 (2015) 7766-7779.
[24] F. Zhang, A. Nicolle, L.L. Xing, S.J. Klippenstein, Proc. Combust. Inst. 36 (2017) 169-177.
[25] Y. Georgievskii, L.B. Harding, S.J. Klippenstein, VaReCoF, Argonne National Laboratory, (2011).
[26] J.A. Miller, S.J. Klippenstein, J. Phys. Chem. A 36 (2006) 10528-10544.
[27] B.E. Poling, J.M. Prausnitz, J.P. O'Connell, The Properties of Gases and Liquids, eth ed.; McGraw-Hill, Boston, MA, 2001.
[28] A.W. Jasper, C.M. Oana, J.A. Miller, Proc. Combust. Inst. 35 (2015) 197-204.

[29] MESS.2016.3.23, http://tcg.cse.anl.gov/papr/codes/mess.html, Y. Georgievskii, S. J. Klippenstein, 2016, Argonne National Laboratory.
[30] Y. Georgievskii, J.A. Miller, M.P. Burke and S.J. Klippenstein, J. Phys. Chem. A 117 (2013) 12146-12154.

Supplemental Material for:

Kinetics of 1-Butyl and 2-Butyl Radical Reactions with Molecular Oxygen: Experiment and Theory

Arkke J. Eskola[1], Timo T. Pekkanen[1], Satya P. Joshi[1], Raimo S. Timonen[1], Stephen J. Klippenstein[2]*

[1]Molecular Science, Department of Chemistry, University of Helsinki, FI-00560 Helsinki, Finland

[2]Argonne National Laboratory, Chemical Sciences and Engineering, Argonne, IL 60439 USA

*Corresponding author:

arkke.eskola@helsinki.fi

Table S1. Conditions and results of the experiments used to measure the bimolecular rate coefficients of *n*-C_4H_9 + O_2 reaction. The shown error limits in k_w are 1σ fitting uncertainties only, while error limits in bimolecular reaction rate coefficients *k* are 1σ fitting uncertainties + estimate of other uncertainties.

T (K)	p_{He} (Torr)	[He] (cm^{-3}) x 10^{16}	[Pr][d] (cm^{-3}) x 10^{12}	[O_2] (cm^{-3}) x 10^{12}	k' (s^{-1})	k_w[f] (s^{-1})	k_w[g] (s^{-1})	k[h] ($cm^3\ s^{-1}$) x 10^{-13}
221[a]	0.42	1.83	33.8	7.73–14.7	76.0–124	10.3±1.41	13.8±7.67	81.5 ± 11.8
221[a]	0.86	3.76	34.2	4.90–15.0	51.7–135	12.0±1.22	12.1±5.00	82.3 ± 9.2
221[a]	1.45	6.35	31.1	6.32–14.3	58.5–151	18.4±1.05	11.9±9.78	88.0 ± 14.2
221[b]	2.35	10.3	26.4	5.70–13.1	85.9–152	23.9±1.72	25.9±4.79	98.3 ± 11.2 [i]
221[b]	3.36	14.7	27.4	5.17–11.9	89.5–163	34.0±1.44	31.1±10.3	101 ± 18.4 [i]
243[a]	0.46	1.81	26.4	5.10–14.4	50.1–116	14.3±0.76	14.6±1.53	72.0 ± 5.3
243[a]	0.95	3.79	28.7	7.46–20.2	64.4–162	15.1±0.66	14.2±3.04	72.4 ± 6.1
243[a]	1.60	6.36	28.7	5.06–16.3	48.0–136	9.31±1.02	10.6±2.98	76.4 ± 6.8
243[b]	3.68	14.6	35.9	6.35–12.5	99.7–138	37.0±1.32	38.9±3.50	83.2 ± 8.6 [i]
298[a]	0.57	1.84	9.01	5.23–13.8	33.5–79.0	8.54±1.62	7.29±2.87	50.9 ± 5.6
298[a]	1.17	3.80	14.6[e]	6.68–22.0	48.0–161	6.26±1.35	7.86±6.68	62.9 ± 7.8
298[a]	1.17	3.81	10.1	7.66–20.9	44.4–128	2.00±2.26	0.35±2.62	60.2 ± 5.0
298[c]	1.18	3.81	25.1	9.75–21.5	72.4–139	12.5±0.65	13.0±1.93	58.1 ± 4.4 [i]
298[c]	1.18	3.82	6.37	9.59–24.2	54.4–146	3.52±0.86	2.05±2.28	57.6 ± 4.5 [i]
298[a]	1.21	3.91	7.08	4.90–13.9	39.0–90.7	4.33±1.70	5.68±3.73	59.1 ± 7.2
298[a]	1.98	6.43	15.6	4.13–15.7	23.4–100	5.26±1.10	3.30±6.83	61.4 ± 10.0
298[b]	3.27	10.6	30.8	7.90–16.4	84.6–130	28.2±1.19	31.4±4.98	64.3 ± 7.7 [i]
298[b]	4.56	14.7	29.9	7.04–17.3	74.7–143	32.0±1.55	31.9±1.83	64.1 ± 4.9 [i]
363[a]	0.70	1.87	14.7	5.97–26.3	25.9–98.3	5.98±1.58	4.08±2.73	35.5 ± 3.5
363[a]	1.43	3.79	10.8	5.54–16.1	30.5–71.9	6.56±0.74	7.44±1.75	41.6 ± 3.7
363[a]	2.47	6.58	19.3	5.98–20.3	37.1–102	7.18±0.99	5.95±3.08	46.4 ± 4.7
363[b]	4.01	10.7	9.77	7.89–24.9	57.8–129	16.1±1.08	18.0±4.67	48.2 ± 5.7 [i]
363[b]	5.58	14.8	10.0	7.76–30.6	59.0–163	15.5±1.12	18.7±3.76	47.5 ± 7.3 [i]
430[c]	0.82	1.84	6.90	8.39–49.5	21.7–103	2.79±1.03	4.31±2.11	20.9 ± 1.7 [i]
430[c]	0.83	1.85	6.95	20.2–39.4	50.1–91.2	7.20±1.12	6.69±1.56	21.2 ± 1.7 [i]

430[c]	1.66	3.73	5.36	7.29–45.4	18.7–103	4.13±1.10	3.70±1.15	22.2 ± 1.5 [i]
504[c]	0.93	1.84	14.2	18.3–40.8	49.7–84.3	17.0±2.31	17.3±3.00	15.9 ± 2.0 [i]
504[c]	1.90	3.70	11.4	17.7–69.1	57.4–152	19.3±2.21	21.2±5.43	17.9 ± 2.3 [i]

[a] Reactor: d = 1.70 cm, stainless steel, halocarbon wax coating.
[b] Reactor: d = 0.80 cm, stainless steel, halocarbon wax coating.
[c] Reactor: d = 1.65 cm, Pyrex, PDMS coating.
[d] Precursor: 1-bromobutane, unless otherwise stated. This precursor was photolyzed with a pulsed ArF exciplex laser. The used pulse energies were between 4 and 50 mJ/pulse.
[e] Precursor: 2-hexanone. This precursor was photolysed with a pulsed ArF exciplex laser. The used pulse energy was 5 mJ/pulse.
[f] Average of measured wall rates.
[g] Wall rate determined from the linear fit y-axis intercept.
[h] A chlorine lamp with a CaF_2 window used for ionization (Cl/CaF_2), unless otherwise stated.
[i] Cl/BaF_2.

Table S2: Stationary Point Energies for the 1- and 2-butyl + O_2 Reactions.

Stationary Point	Energy (kcal/mol)[a]	Energy (kcal/mol)[b]
$1\text{-}C_4H_9OO$	-33.54 (-33.2)	
$1\text{-}C_4H_9OO = 1\text{-}C_4H_8 + HO_2$	-2.43 (-3.2)	
$2\text{-}C_4H_9OO$		-34.55 (-35.2)
$2\text{-}C_4H_9OO = 1\text{-}C_4H_8 + HO_2$		-3.79 (-4.5)
$2\text{-}C_4H_9OO = 2\text{-}C_4H_8 + HO_2$		-4.26 (-4.3)

[a] Relative to $1\text{-}C_4H_9 + O_2$. The primary entries are the CCSD(T)/CBS//B2PLYP-D3/cc-pVTZ values including $C_2H_5 + O_2$ based corrections, while the numbers in parentheses are the values from Ref. [1]. All values include zero-point corrections.

[b] Relative to $2\text{-}C_4H_9 + O_2$. The primary entries are the CCSD(T)/CBS//B2PLYP-D3/cc-pVTZ values including $C_2H_5 + O_2$ based corrections, while the numbers in parentheses are the values from Ref. [1] All values include zero-point corrections.

Table S3. Conditions and results of the experiments used to measure the bimolecular rate coefficients of *s*-C_4H_9 + O_2 reaction. The shown error limits in k_w are 1σ fitting uncertainties only, while error limits in bimolecular reaction rate coefficients k are 1σ fitting uncertainties + estimate of other uncertainties.

T (K)	p_{He} (Torr)	[He] (cm^{-3}) x 10^{16}	[Pr][d] (cm^{-3}) x 10^{12}	[O_2] (cm^{-3}) x 10^{12}	k' (s^{-1})	k_w[e] (s^{-1})	k_w[f] (s^{-1})	k[g] ($cm^3\ s^{-1}$) x 10^{-13}
205[a]	0.38	1.79	83.3	2.25–7.99	44.6–149	27.1±2.46	16.3±9.74	151 ± 27.9
205[a]	0.79	3.71	83.3	2.04–6.92	48.7–132	26.5±2.04	20.9±5.93	148 ± 21.1
205[a]	1.34	6.31	66.4	2.45–6.72	59.2–130	17.1±1.51	16.4±4.31	165 ± 17.6
205[b]	2.08	9.79	71.2	0.99–4.99	80.0–202	46.6±6.74	51.4±9.31	304 ± 46.4
205[b]	3.08	14.5	88.6	1.75–5.08	102–195	53.3±3.17	54.2±3.97	281 ± 26.8
243[a]	0.45	1.81	-	3.05–8.66	48.8–109	6.98±1.70	7.81±3.42	114 ± 12.3
243[a]	0.46	1.84	68.4	3.00–10.6	61.3–185	28.7±1.87	24.9±4.76	142 ± 14.9
243[a]	0.95	3.77	71.3	5.98–13.7	67.5–170	13.0±1.46	12.1±12.4	115 ± 20.2
243[a]	0.96	3.80	-	2.66–9.92	50.4–149	11.2±2.24	11.1±5.21	113 ± 15.4
243[b]	1.32	5.25	68.4	2.47–9.56	79.5–207	36.0±3.06	39.0±6.53	184 ± 20.7
243[a]	1.60	6.36	79.3	3.48–11.7	55.1–155	13.0±1.50	15.5±8.76	124 ± 19.7
243[a]	1.61	6.39	-	3.70–9.58	64.5–137	15.2±1.46	16.2±1.52	129 ± 9.2
243[b]	1.66	6.60	14.5	2.89–10.2	91.7–224	33.2±1.62	36.3±5.02	188 ± 18.5
243[b]	2.64	10.5	90.0	2.40–8.64	95.4–213	31.2±1.27	38.4±7.37	202 ± 23.9
243[b]	3.68	14.6	92.8	2.15–7.11	91.4–197	32.3±1.33	32.9±1.30	243 ± 19.3
243[b]	3.69	14.7	173	1.34–5.21	70.1–135	29.7±1.52	33.3±4.31	208 ± 25.5
298[a]	0.27	0.87	53.4	3.22–14.1	32.0–135	5.17±3.33	4.36±1.87	94.0 ± 7.2
298[a]	0.56	1.83	58.0	5.38–15.8	57.2–173	10.3±1.54	8.67±5.27	103 ± 10.4
298[c]	0.57	1.86	66.1	3.93–30.7	63.2–319	31.2±1.27	30.3±4.03	95.2 ± 7.3
298[c]	1.17	3.80	78.7	1.40–8.21	26.9–98.0	3.50±1.05	5.38±2.77	109 ± 11.6
298[c]	1.17	3.80	66.4	5.38–9.72	91.9–123	29.4±1.10	32.7±6.03	98.4 ± 13.9
298[a]	1.18	3.81	60.7	4.33–10.6	58.1–127	8.97±1.16	9.71±4.75	106 ± 12.4
298[b]	1.67	5.41	60.2	2.24–7.97	63.5–145	20.7±1.50	26.6±5.48	150 ± 18.5
298[b]	1.89	6.11	40.2	2.76–8.28	70.2–156	19.6±1.69	21.3±7.33	168 ± 23.1
298[b]	1.95	6.33	43.7	3.47–8.76	71.9–144	19.5±1.70	20.2±7.03	151 ± 20.1
298[a]	1.97	6.39	57.6	3.07–9.83	45.3–123	7.88±1.49	10.2±3.03	115 ± 11.0
298[b]	3.27	10.6	78.9	1.73–12.5	67.7–209	17.6±0.75	31.7±7.56	140 ± 17.6

298[b]	3.29	10.7	55.5	3.41–10.3	74.3–140	24.9±1.46	24.1±1.64	147 ± 10.1
298[b]	3.36	10.9	39.3	2.69–12.1	59.6–159	30.3±1.49	31.5±7.29	114 ± 16.1
298[b]	4.57	14.8	73.5	0.68–10.6	41.2–192	26.1±1.35	26.8±2.58	152 ± 12.3
298[b]	4.58	14.8	58.4	2.59–6.76	58.5–108	24.3±1.82	30.9±9.76	131 ± 31.2
363[a]	0.36	0.96	35.0	4.17–22.4	26.2–136	7.15±1.47	6.09±5.32	56.4 ± 6.7
363[a]	0.70	1.87	39.6	4.16–11.7	30.3–84.2	3.49±1.72	2.50±1.91	68.1 ± 6.0
363[a]	0.70	1.87	49.2	4.07–11.7	33.8–71.0	3.99±1.12	6.69±4.00	59.1 ± 7.9
363[a]	1.45	3.87	41.5	3.14–10.9	31.4–79.8	5.54±0.78	7.57±1.54	67.1 ± 5.8
363[a]	2.41	6.42	42.3	3.48–12.7	35.0–92.7	9.47±0.80	10.8±1.74	67.1 ± 5.7
363[b]	4.02	10.7	53.9	4.59–12.2	60.0–131	24.8±2.07	23.3±2.99	89.7 ± 8.1
363[b]	5.16	13.7	55.5	2.65–13.9	51.5–143	20.3±1.44	19.1±2.14	89.9 ± 6.8
363[b]	5.58	14.8	60.7	3.29–17.5	54.5–187	18.8±1.27	21.6±2.53	96.1 ± 7.7
420[c]	0.41	0.95	23.5	12.8–50.7	44.6–125	17.7±1.52	16.3±7.04	22.1 ± 3.3
420[c]	0.81	1.85	24.8	8.36–32.8	41.3–104	15.8±0.99	16.1±2.46	26.3 ± 2.6
420[c]	1.64	3.76	34.2	7.25–34.9	36.4–128	15.3±0.80	14.5±1.59	31.8 ± 2.5
494[c]	0.44	0.86	35.2	13.8–78.5	31.6–126	14.8±1.02	12.4±4.12	13.8 ± 1.6
494[c]	0.90	1.76	47.8	11.9–68.0	32.0–131	15.2±0.77	14.7±1.84	17.0 ± 1.5
494[c]	1.83	3.57	36.8	13.6–53.3	40.0–109	16.1±1.12	16.4±1.14	17.6 ± 1.3

[a] Reactor: d = 1.70 cm, stainless steel, halocarbon wax coating.
[b] Reactor: d = 0.80 cm, stainless steel, halocarbon wax coating.
[c] Reactor: d = 1.65 cm, Pyrex, PDMS coating.
[d] Precursor: 2-bromobutane. This precursor was photolyzed with a pulsed KrF exciplex laser. The used pulse energies were between 50 and 200 mJ/pulse.
[e] Average of measured wall rates.
[f] Wall rate determined from the linear fit y-axis intercept.
[g] A chlorine lamp with a BaF_2 window used for ionization.

Table S4: Modified Arrhenius representations of the rate coefficients for the 1- and 2-butyl + O_2 reaction systems (in ChemKin PLOG format).

These rate coefficients are tabulated for the case of an N_2 collider. Furthermore, the predictions are based on a model that employs an entrance flux (i.e., high pressure recombination rate) that has been reduced by a factor of 0.8. The two numbers after "MAE" denote the mean and max absolute errors, with the latter defined as mean(abs((theory - fit)/theory)).

1-butyl + O_2

R = 1-C_4H_9 + O_2 W1 = 1-$C_4H_9O_2$, P1 = 1-C_4H_8 + O_2

```
W1=P1                    7.78E+33    -6.46   39520.0
 PLOG/1.000E-02  7.52E+47   -11.91   38000.0/      ! fit btw. 500 and 1435 K with MAE of 10.7%, 19.2%
 PLOG/2.000E-02  6.08E+46   -11.47   38050.0/      ! fit btw. 500 and 1500 K with MAE of 11.5%, 21.0%
 PLOG/5.000E-02  1.14E+48   -11.71   39390.0/      ! fit btw. 500 and 1500 K with MAE of 10.6%, 19.4%
 PLOG/1.000E-01  6.96E+48   -11.84   40350.0/      ! fit btw. 500 and 1500 K with MAE of 9.6%, 18.5%
 PLOG/2.000E-01  5.75E+46   -11.11   40030.0/      ! fit btw. 500 and 1625 K with MAE of 10.5%, 23.9%
 PLOG/5.000E-01  1.82E+47   -11.12   41130.0/      ! fit btw. 500 and 1625 K with MAE of 8.8%, 21.7%
 PLOG/1.000E+00  1.62E+47   -11.00   41770.0/      ! fit btw. 500 and 1625 K with MAE of 7.4%, 19.4%
 PLOG/2.000E+00  4.01E+44   -10.12   41220.0/      ! fit btw. 500 and 1750 K with MAE of 8.4%, 21.2%
 PLOG/5.000E+00  7.85E+41    -9.19   40820.0/      ! fit btw. 500 and 1875 K with MAE of 8.3%, 20.5%
 PLOG/1.000E+01  8.41E+40    -8.81   41000.0/      ! fit btw. 500 and 1875 K with MAE of 7.3%, 16.4%
 PLOG/2.000E+01  2.37E+38    -7.96   40390.0/      ! fit btw. 500 and 2000 K with MAE of 7.6%, 15.5%
 PLOG/5.000E+01  1.36E+36    -7.19   40080.0/      ! fit btw. 500 and 2000 K with MAE of 6.9%, 14.5%
 PLOG/1.000E+02  7.78E+33    -6.46   39520.0/      ! fit btw. 500 and 2000 K with MAE of 6.8%, 17.6%

R=W1                     4.39E+42    -9.22   12350.0
 PLOG/1.000E-02  2.25E+69   -18.69   15480.0/      ! fit btw. 500 and 1435 K with MAE of 1.2%, 3.5%
 PLOG/2.000E-02  2.18E+69   -18.55   16090.0/      ! fit btw. 500 and 1500 K with MAE of 1.7%, 4.8%
 PLOG/5.000E-02  2.81E+68   -18.11   16570.0/      ! fit btw. 500 and 1500 K with MAE of 1.8%, 5.0%
 PLOG/1.000E-01  3.18E+67   -17.70   16850.0/      ! fit btw. 500 and 1500 K with MAE of 2.2%, 6.1%
 PLOG/2.000E-01  1.23E+67   -17.45   17400.0/      ! fit btw. 500 and 1625 K with MAE of 3.2%, 9.1%
 PLOG/5.000E-01  8.60E+64   -16.64   17420.0/      ! fit btw. 500 and 1625 K with MAE of 4.0%, 11.2%
 PLOG/1.000E+00  6.57E+62   -15.88   17230.0/      ! fit btw. 500 and 1625 K with MAE of 4.9%, 13.2%
 PLOG/2.000E+00  3.16E+61   -15.37   17400.0/      ! fit btw. 500 and 1750 K with MAE of 6.5%, 17.5%
 PLOG/5.000E+00  7.99E+58   -14.45   17210.0/      ! fit btw. 500 and 1875 K with MAE of 8.8%, 22.8%
 PLOG/1.000E+01  2.54E+55   -13.30   16300.0/      ! fit btw. 500 and 1875 K with MAE of 10.0%, 24.7%
 PLOG/2.000E+01  1.04E+53   -12.49   15880.0/      ! fit btw. 500 and 2000 K with MAE of 12.2%, 28.7%
 PLOG/5.000E+01  2.08E+47   -10.68   14020.0/      ! fit btw. 500 and 2000 K with MAE of 13.4%, 30.8%
 PLOG/1.000E+02  4.39E+42    -9.22   12350.0/      ! fit btw. 500 and 2000 K with MAE of 13.9%, 32.4%

R=P1                     6.29E+20    -2.61   15220.0
 PLOG/1.000E-02  3.32E+04    1.73   -2195.0/      ! fit btw. 500 and 2000 K with MAE of 5.4%, 18.1%
 PLOG/2.000E-02  5.61E+05    1.38   -1312.0/      ! fit btw. 500 and 2000 K with MAE of 6.4%, 20.5%
 PLOG/5.000E-02  4.78E+07    0.84    101.0/       ! fit btw. 500 and 2000 K with MAE of 7.7%, 23.2%
 PLOG/1.000E-01  2.33E+09    0.37    1364.0/      ! fit btw. 500 and 2000 K with MAE of 8.6%, 24.7%
 PLOG/2.000E-01  1.71E+11   -0.15    2791.0/      ! fit btw. 500 and 2000 K with MAE of 9.3%, 25.3%
 PLOG/5.000E-01  7.93E+13   -0.89    4905.0/      ! fit btw. 500 and 2000 K with MAE of 9.9%, 24.2%
 PLOG/1.000E+00  9.50E+15   -1.47    6636.0/      ! fit btw. 500 and 2000 K with MAE of 10.0%, 21.5%
 PLOG/2.000E+00  9.92E+17   -2.02    8421.0/      ! fit btw. 500 and 2000 K with MAE of 9.6%, 19.2%
 PLOG/5.000E+00  2.17E+20   -2.65   10740.0/      ! fit btw. 500 and 2000 K with MAE of 8.2%, 18.2%
 PLOG/1.000E+01  4.36E+21   -2.99   12330.0/      ! fit btw. 500 and 2000 K with MAE of 6.8%, 16.1%
 PLOG/2.000E+01  2.23E+22   -3.15   13670.0/      ! fit btw. 500 and 2000 K with MAE of 6.4%, 12.5%
 PLOG/5.000E+01  1.19E+22   -3.02   14860.0/      ! fit btw. 500 and 2000 K with MAE of 6.7%, 17.7%
 PLOG/1.000E+02  6.29E+20   -2.61   15220.0/      ! fit btw. 500 and 2000 K with MAE of 8.4%, 24.4%
```

2-butyl + O_2

R = 2-C_4H_9 + O_2 W1 = 2-$C_4H_9O_2$, P1 = 1-C_4H_8 + O_2, P2 = 2-C_4H_8 + O_2

```
W1=P1                    3.73E+24    -3.16   36270.0
 PLOG/1.000E-02  6.37E+40   -9.37   35530.0/      ! fit btw. 500 and 1188 K with MAE of 13.2%, 24.6%
 PLOG/2.000E-02  5.17E+42   -9.84   36880.0/      ! fit btw. 500 and 1188 K with MAE of 12.2%, 23.5%
 PLOG/5.000E-02  1.75E+39   -8.63   36190.0/      ! fit btw. 500 and 1250 K with MAE of 14.5%, 27.5%
```

```
 PLOG/1.000E-01   2.50E+41     -9.17   37720.0/                ! fit btw. 500 and 1250 K with MAE of 13.1%, 25.7%
 PLOG/2.000E-01   7.21E+37     -7.99   36840.0/                ! fit btw. 500 and 1315 K with MAE of 15.0%, 29.7%
 PLOG/5.000E-01   2.92E+40     -8.63   38830.0/                ! fit btw. 500 and 1315 K with MAE of 12.4%, 26.1%
 PLOG/1.000E+00   4.71E+37     -7.67   38280.0/                ! fit btw. 500 and 1375 K with MAE of 13.4%, 27.8%
 PLOG/2.000E+00   1.97E+35     -6.85   37890.0/                ! fit btw. 500 and 1435 K with MAE of 13.5%, 28.9%
 PLOG/5.000E+00   2.81E+33     -6.17   37920.0/                ! fit btw. 500 and 1500 K with MAE of 12.5%, 28.6%
 PLOG/1.000E+01   2.41E+31     -5.46   37610.0/                ! fit btw. 500 and 1563 K with MAE of 11.9%, 28.2%
 PLOG/2.000E+01   3.25E+29     -4.81   37340.0/                ! fit btw. 500 and 1625 K with MAE of 11.2%, 26.9%
 PLOG/5.000E+01   5.42E+27     -4.17   37250.0/                ! fit btw. 500 and 1688 K with MAE of 9.3%, 22.7%
 PLOG/1.000E+02   3.73E+24     -3.16   36270.0/                ! fit btw. 500 and 1813 K with MAE of 9.9%, 23.5%

W1=P2                         2.85E+26     -4.39   35620.0
 PLOG/1.000E-02   9.80E+45    -11.39   37360.0/                ! fit btw. 500 and 1188 K with MAE of 10.0%, 19.1%
 PLOG/2.000E-02   1.31E+47    -11.64   38340.0/                ! fit btw. 500 and 1188 K with MAE of 9.3%, 18.3%
 PLOG/5.000E-02   1.05E+44    -10.56   37750.0/                ! fit btw. 500 and 1250 K with MAE of 11.0%, 21.4%
 PLOG/1.000E-01   1.48E+45    -10.81   38800.0/                ! fit btw. 500 and 1250 K with MAE of 9.8%, 19.9%
 PLOG/2.000E-01   9.72E+41     -9.75   38010.0/                ! fit btw. 500 and 1315 K with MAE of 11.3%, 23.2%
 PLOG/5.000E-01   1.39E+43     -9.98   39280.0/                ! fit btw. 500 and 1315 K with MAE of 9.2%, 20.1%
 PLOG/1.000E+00   2.56E+40     -9.06   38670.0/                ! fit btw. 500 and 1375 K with MAE of 9.8%, 21.4%
 PLOG/2.000E+00   9.01E+37     -8.23   38150.0/                ! fit btw. 500 and 1435 K with MAE of 9.8%, 22.3%
 PLOG/5.000E+00   4.63E+35     -7.43   37860.0/                ! fit btw. 500 and 1500 K with MAE of 9.1%, 21.9%
 PLOG/1.000E+01   2.85E+33     -6.69   37380.0/                ! fit btw. 500 and 1563 K with MAE of 8.7%, 21.6%
 PLOG/2.000E+01   2.65E+31     -6.01   36940.0/                ! fit btw. 500 and 1625 K with MAE of 8.1%, 20.5%
 PLOG/5.000E+01   2.08E+29     -5.30   36560.0/                ! fit btw. 500 and 1688 K with MAE of 7.1%, 17.0%
 PLOG/1.000E+02   2.85E+26     -4.39   35620.0/                ! fit btw. 500 and 1813 K with MAE of 7.6%, 17.9%


R=W1                          1.88E+25     -4.05    3873.0
 PLOG/1.000E-02   1.09E+35     -8.17    1546.0/                ! fit btw. 500 and 1188 K with MAE of 12.2%, 21.9%
 PLOG/2.000E-02   4.52E+37     -8.85    3094.0/                ! fit btw. 500 and 1188 K with MAE of 11.3%, 20.9%
 PLOG/5.000E-02   6.90E+35     -8.15    2986.0/                ! fit btw. 500 and 1250 K with MAE of 12.8%, 23.6%
 PLOG/1.000E-01   1.90E+38     -8.78    4555.0/                ! fit btw. 500 and 1250 K with MAE of 11.5%, 22.1%
 PLOG/2.000E-01   8.23E+35     -7.96    4100.0/                ! fit btw. 500 and 1315 K with MAE of 12.8%, 25.0%
 PLOG/5.000E-01   3.02E+38     -8.60    5971.0/                ! fit btw. 500 and 1315 K with MAE of 10.6%, 22.0%
 PLOG/1.000E+00   2.67E+36     -7.88    5664.0/                ! fit btw. 500 and 1375 K with MAE of 11.2%, 22.9%
 PLOG/2.000E+00   4.08E+34     -7.24    5439.0/                ! fit btw. 500 and 1435 K with MAE of 11.1%, 23.5%
 PLOG/5.000E+00   1.18E+33     -6.66    5486.0/                ! fit btw. 500 and 1500 K with MAE of 10.0%, 22.9%
 PLOG/1.000E+01   2.01E+31     -6.05    5209.0/                ! fit btw. 500 and 1563 K with MAE of 9.4%, 22.4%
 PLOG/2.000E+01   4.31E+29     -5.48    4935.0/                ! fit btw. 500 and 1625 K with MAE of 8.7%, 21.0%
 PLOG/5.000E+01   8.21E+27     -4.89    4725.0/                ! fit btw. 500 and 1688 K with MAE of 6.8%, 17.6%
 PLOG/1.000E+02   1.88E+25     -4.05    3873.0/                ! fit btw. 500 and 1813 K with MAE of 7.0%, 18.0%

R=P1                          5.83E+21     -2.44   15500.0
 PLOG/1.000E-02   1.42E+02      2.91   -2787.0/                ! fit btw. 500 and 2000 K with MAE of 2.3%, 7.3%
 PLOG/2.000E-02   1.37E+03      2.64   -2087.0/                ! fit btw. 500 and 2000 K with MAE of 2.6%, 9.8%
 PLOG/5.000E-02   5.59E+04      2.18    -924.6/                ! fit btw. 500 and 2000 K with MAE of 3.2%, 13.3%
 PLOG/1.000E-01   1.66E+06      1.77    153.7/                 ! fit btw. 500 and 2000 K with MAE of 4.0%, 15.6%
 PLOG/2.000E-01   8.15E+07      1.30    1415.0/                ! fit btw. 500 and 2000 K with MAE of 4.8%, 17.5%
 PLOG/5.000E-01   2.87E+10      0.59    3360.0/                ! fit btw. 500 and 2000 K with MAE of 5.7%, 18.4%
 PLOG/1.000E+00   3.69E+12     -0.00    5024.0/                ! fit btw. 500 and 2000 K with MAE of 6.2%, 17.5%
 PLOG/2.000E+00   5.66E+14     -0.61    6816.0/                ! fit btw. 500 and 2000 K with MAE of 6.3%, 14.9%
 PLOG/5.000E+00   3.70E+17     -1.38    9278.0/                ! fit btw. 500 and 2000 K with MAE of 5.7%, 10.9%
 PLOG/1.000E+01   2.83E+19     -1.89   11110.0/                ! fit btw. 500 and 2000 K with MAE of 4.9%, 9.6%
 PLOG/2.000E+01   8.44E+20     -2.28   12790.0/                ! fit btw. 500 and 2000 K with MAE of 4.6%, 8.5%
 PLOG/5.000E+01   8.58E+21     -2.53   14590.0/                ! fit btw. 500 and 2000 K with MAE of 5.1%, 17.9%
 PLOG/1.000E+02   5.83E+21     -2.44   15500.0/                ! fit btw. 500 and 2000 K with MAE of 7.4%, 25.8%

R=P2                          1.64E+26     -4.47   16520.0
 PLOG/1.000E-02   1.56E+08      0.41   -1514.0/                ! fit btw. 500 and 2000 K with MAE of 2.9%, 12.2%
 PLOG/2.000E-02   2.27E+09      0.08    -666.1/                ! fit btw. 500 and 2000 K with MAE of 3.6%, 14.4%
 PLOG/5.000E-02   1.55E+11     -0.43    690.9/                 ! fit btw. 500 and 2000 K with MAE of 4.5%, 17.0%
 PLOG/1.000E-01   6.40E+12     -0.88    1907.0/                ! fit btw. 500 and 2000 K with MAE of 5.3%, 18.5%
 PLOG/2.000E-01   4.02E+14     -1.38    3289.0/                ! fit btw. 500 and 2000 K with MAE of 6.0%, 19.1%
 PLOG/5.000E-01   1.62E+17     -2.11    5351.0/                ! fit btw. 500 and 2000 K with MAE of 6.6%, 18.3%
 PLOG/1.000E+00   1.91E+19     -2.68    7058.0/                ! fit btw. 500 and 2000 K with MAE of 6.6%, 15.9%
 PLOG/2.000E+00   2.21E+21     -3.25    8842.0/                ! fit btw. 500 and 2000 K with MAE of 6.4%, 12.0%
 PLOG/5.000E+00   7.18E+23     -3.94   11210.0/                ! fit btw. 500 and 2000 K with MAE of 5.5%, 10.4%
 PLOG/1.000E+01   2.54E+25     -4.35   12890.0/                ! fit btw. 500 and 2000 K with MAE of 4.8%, 9.2%
 PLOG/2.000E+01   2.93E+26     -4.62   14380.0/                ! fit btw. 500 and 2000 K with MAE of 4.9%, 11.7%
 PLOG/5.000E+01   7.20E+26     -4.69   15870.0/                ! fit btw. 500 and 2000 K with MAE of 6.1%, 22.3%
 PLOG/1.000E+02   1.64E+26     -4.47   16520.0/                ! fit btw. 500 and 2000 K with MAE of 9.0%, 29.3%
```

Details of the Theoretical Methodology

Stationary Point Properties

The B2PLYP-D3 functional was used in the evaluation of the rovibrational properties because it accurately reproduces CCSD(T) properties for related stationary points in the $C_2H_5 + O_2$ system. In particular, for the three stationary points of relevance to the present work ($C_2H_5 + O_2$, $C_2H_5O_2$, $C_2H_5O_2 \rightarrow C_2H_4 + HO_2$), the discrepancy between the canonical partition functions calculated with the B2PLYP-D3/cc-pVTZ and CCSD(T)/cc-pVTZ two methods is less than 4% for all $T < 2000$ K.

Each of the rovibrational analyses began with a determination of the torsional minimum geometry. The torsional potentials from the M06-2X/cc-pVTZ analysis were renormalized to reproduce the corresponding B2PLYP-D3/cc-pVTZ harmonic frequencies.

VRC-TST Analysis

The VRC-TST approach invokes a separation into the vibrational modes of the two reacting fragments, which are considered as more or less invariant from their values at infinite separation, and the relative and overall rotational modes, whose character is rapidly changing in the transition state region. The contribution from the "transitional" modes is obtained via crude Monte Carlo integration over the configurational integrals defining the transition state partition function. The transition state dividing surface is obtained by variational optimization of the *position* (relative to the fragment framework) and *separation* of pivot points on each of the fragments, with these pivot points defining the rotational motions of the fragments.

Here, center-of-mass pivot points were employed at long range, while at short range two pivot points were included for both C_4H_9 and O_2. For the butyl radicals these two pivot points are displaced away from the radical C atom in the direction of the two lobes of the radical orbital. For O_2 the pivot points are displaced along the molecular axis. The configurational integrals were converged to about 10% accuracy at the 2σ level.

For radical-radical reactions, single reference based electronic structure methods generally do not provide an accurate description of the energetics in the TS regime. Thus, we instead focus on CASPT2 and MRCI+Q (internally contracted multi-reference configuration interaction with single and double excitations including Davidson corrections) calculations, which typically provide consistent high accuracy estimates for the radical-radical interaction energies. For radical + O_2 reactions, we find that a 7-electron, 5-orbital (7e,5o) active space consisting of the (6e,4o) π space of O_2, provides a good description of the changing interactions along the recombination path. This active space is the smallest one to provide a semiquantitative description of the interactions along the recombination path for radical + O_2 reactions.

For the present butyl + O_2 reactions (and for R + O_2 reactions in general), there is considerable discordancy in the CASPT2 and MRCI+Q evaluated minimum energy paths (MEPs) (cf. Figs. S1 and S2). In contrast, the various multireference methods yield a fairly consistent description of the splitting between the attractive ground doublet state, and the repulsive excited quartet state. Furthermore, traditional CCSD(T) based calculations of the interaction energies for the quartet state are expected to be highly accurate. Thus, we employ an alternative scheme that couples the multireference based evaluation of the spin-splitting with CCSD(T)/CBS evaluations of the quartet energies.

As illustrated in Figs. S1 and S2, the spin-splitting based scheme results in greatly increased consistency of the predicted MEP. Furthermore, for the IPEA shifted results [2] there is relatively little deviation between the direct and spin-splitting based results, and this result tends to lie between the other two. Thus, the IPEA shifted (by 0.25) CASPT2 method is used in the global sampling and to define the one-dimensional corrections.

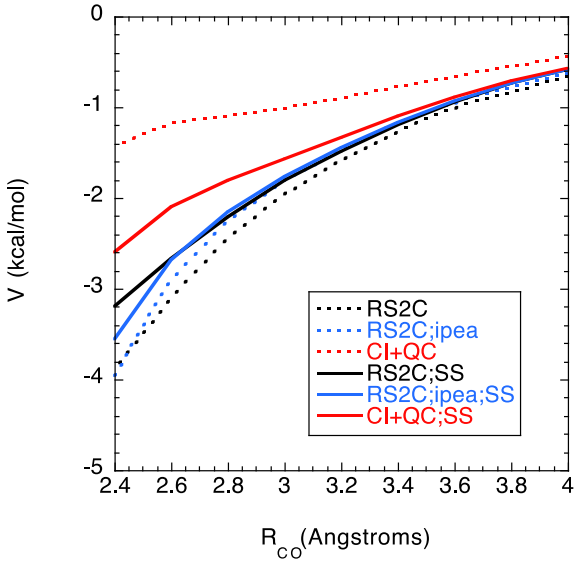

Fig. S1. Plot of the CASPT2 (RS2C), IPEA shifted CASPT2 (RS2C;ipea), and MRCI+Q (CI+QC) predictions of the 1-butyl + O_2 interaction energies along an approximate MEP. The dashed lines denote the direct calculations of the doublet state interaction energies, while the solid lines denote their derivation from the spin-splitting approach.

One-dimensional corrections for limitations in the CASPT2/cc-pVDZ methodology are evaluated along an approximate MEP. These evaluations involve CASPT2/CBS(TZ,QZ) calculations of the doublet and quartet state energies coupled with CCSD(T)-F12/cc-pVTZ-F12 energies of the quartet state energies:

$$E_{1d\_Correction} = {}^{2}\text{CASPT2/CBS} - {}^{4}\text{CASPT2/CBS} + \text{CCSD(T)-F12/cc-pVTZ-F12} - \text{CASPT2/cc-pVDZ}$$

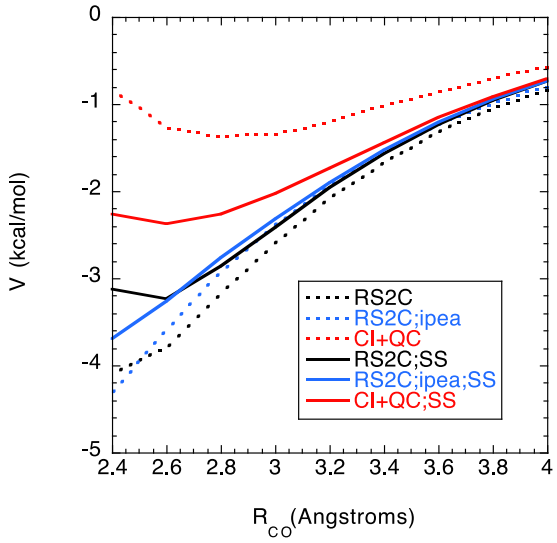

Fig. S2. Plot of the CASPT2 (RS2C), ipea shifted CASPT2 (RS2C;ipea), and MRCI+Q (CI+QC) predictions of the 2-butyl + O_2 interaction energies along an approximate MEP. The dashed lines denote the direct calculations of the doublet state interaction energies, while the solid lines denote their derivation from the spin-splitting approach.

The corrections to the CASPT2/cc-pVDZ direct sampling must also account for geometry relaxation of the fragments, which becomes very important at shorter separations. Because the transition state moves to shorter separations with increasing temperatures, these geometry relaxation effects are particularly important at high temperature. In this study, we evaluated the geometry relaxation correction at the CASPT2(7e,5o)/aug-cc-VDZ level for the RCO distinguished coordinate MEPs for 1- and 2-butyl + O_2.

During the course of this work, it was observed that this correction was fairly strongly dependent on the OOCC torsional coordinate. This dependence is illustrated in Figs. S3 and S4 for 1-butyl and 2-butyl + O_2, respectively. The torsional dependence is particularly strong for 1-butyl, where its neglect could lead to more than a factor of two error in the rate prediction. To account for this dependence, we incorporated a two-dimensional geometry relaxation correction in addition to the one-dimensional method correction, with the extra dimension being the OOCC torsional angle.

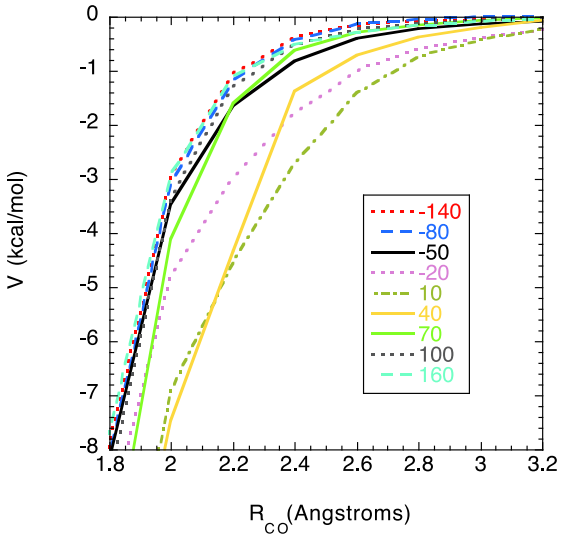

Fig. S3. Plot of the CASPT2/aug-cc-pVDZ evaluated geometry relaxation correction along the R_{CO} distinguished coordinate MEP for 1-butyl + O_2. The numerical values in the label denote different values of the OOCC torsional angle.

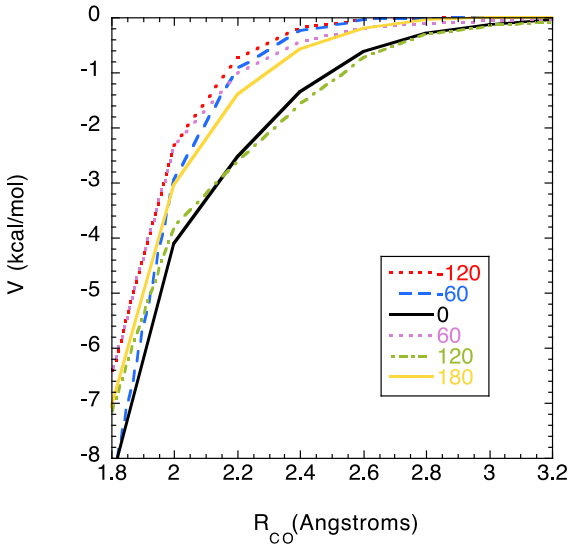

Fig. S4. Plot of the CASPT2/aug-cc-pVDZ evaluated geometry relaxation correction along the R_{CO} distinguished coordinate MEP for 2-butyl + O_2. The numerical values in the label denote different values of the OOCC torsional angle.

The MEPs for the 1 and 2-butyl + O_2 reaction are contrasted in Fig. S5, where they are seen to be nearly identical down to about 3.2 Å, at which point the 2-butyl MEP becomes modestly more attractive.

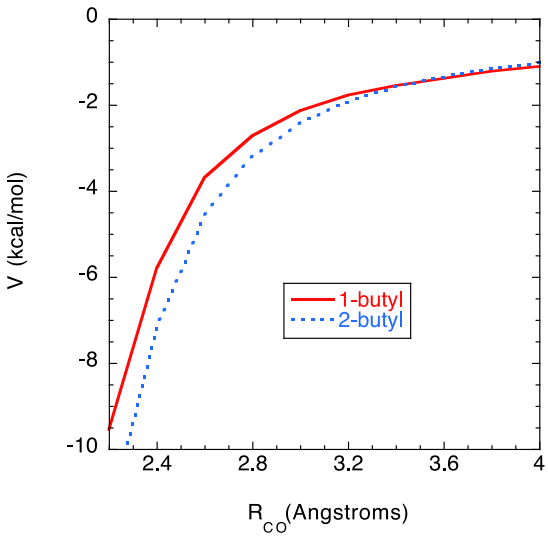

Fig. S5 Plot of the distinguished coordinate (R_{CO}) MEPs for O_2 adding to 1- and 2-butyl radicals.

In addition to mapping the MEP we have also mapped the vibrational frequencies along the 1-butyl + O_2 MEP at the CASPT2(7,5)/aug-cc-pVDZ level. These calculations indicate that the total ZPE change for the conserved vibrational modes is negligible, aside perhaps from the torsional mode, whose variations are difficult to disentangle from the transitional modes. While the ZPE change for the transitional modes is more substantial, our experience is that, at least at the harmonic level, the classical treatment of the transitional modes (as required by the present VRC-TST machinery) fairly accurately reproduces a quantized harmonic oscillator treatment of the ZPE changes.

Sensitivity of Predictions to Uncertain Parameters

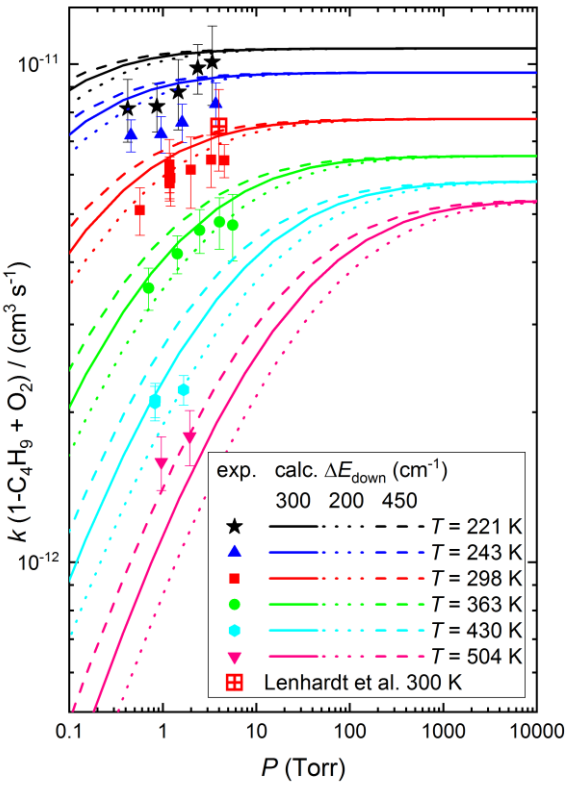

Figure S6. Plot of the experimentally observed (symbols) and theoretically predicted (lines) bimolecular rate coefficients for the 1-butyl + O_2 reaction. The theoretical predictions employ different values for the parameter denoting the average downwards energy transferred at room temperature. The solid lines employ the reference value of 300 cm^{-1}, while the dotted and dashed lines employ values of 200 and 450 cm^{-1}, respectively.

Some sense of the uncertainty in the bimolecular reaction rate coefficient predictions can be obtained by exploring the variation in the predictions with estimated uncertainties in the key parameters. Here, we use an estimated uncertainty of a factor of 1.5 in the parameter specifying the average downwards energy transfer at room temperature to explore the dependence on energy transfer rates. Meanwhile, the stationary point predictions are estimated to have an uncertainty of about 0.4 kcal/mol. We explore the dependence on the barrier heights and the well depths, separately. We estimate an uncertainty in the high

pressure limit rate constants of about 30%. Each of these uncertainty estimates is meant to correlate roughly with a 2σ range of uncertainties.

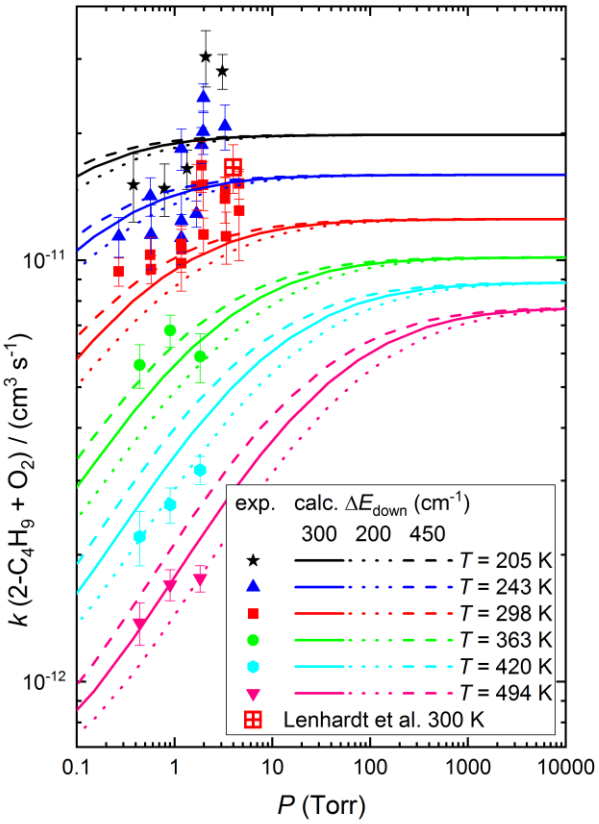

Figure S7. Plot of the experimentally observed (symbols) and theoretically predicted (lines) bimolecular rate coefficients for the 2-butyl + O_2 reaction. The theoretical predictions employ different values for the parameter denoting the average downwards energy transferred at room temperature. The solid lines employ the reference value of 300 cm^{-1}, while the dotted and dashed lines employ values of 200 and 450 cm^{-1}, respectively.

The sensitivities of the predictions for the 1-butyl + O_2 and 2-butyl + O_2 bimolecular reaction rate coefficients to the average downwards energy transfer are illustrated in Figs. S6 and S7, respectively. Over the experimentally studied range of temperature and pressure, the uncertainties in this parameter map into rate coefficient variations of about 20% or less.

For the 1-butyl + O_2 case in Fig. S6, we also employed a modified high pressure rate constant, i.e., one that has been reduced by a factor of 0.8. This reduction greatly decreases the discrepancy between theory and experiment, particularly at lower temperatures. Indeed, with this reduction, the predictions for the 1-butyl + O_2 bimolecular rate coefficient are essentially within the error bars of the experiment under all conditions.

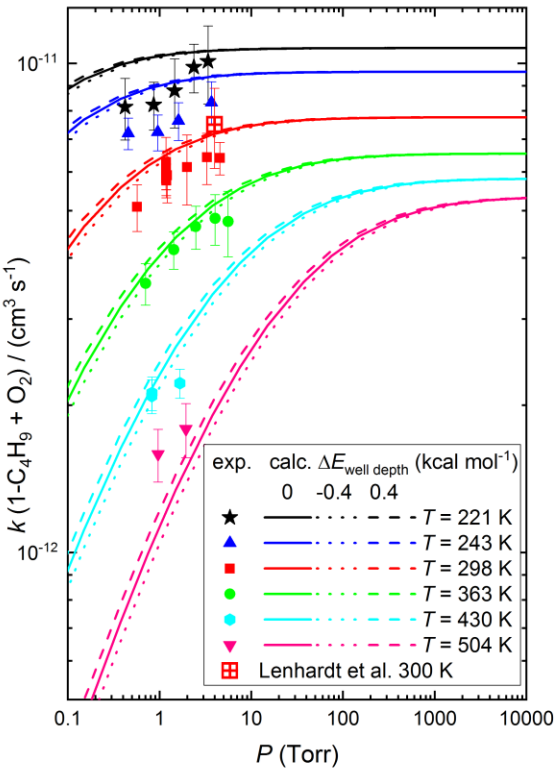

Figure S8. Plot of the experimentally observed (symbols) and theoretically predicted (lines) bimolecular rate coefficients for the 1-butyl + O_2 reaction. The theoretical predictions employ different values for the 1-$C_4H_9O_2$ well depth. The solid lines employ the reference values, while the dotted and dashed lines employ values shifted up and down by 0.4 kcal/mol, respectively.

The plots in Figs. S8 and S9 illustrate the sensitivity of the predictions for the 1-butyl + O_2 and 2-butyl + O_2 bimolecular reaction rate coefficients to variations in the $C_4H_9O_2$ well depths. Notably, the variation

in the well depths within their uncertainty range maps into only a 5% variation in the bimolecular rate predictions.

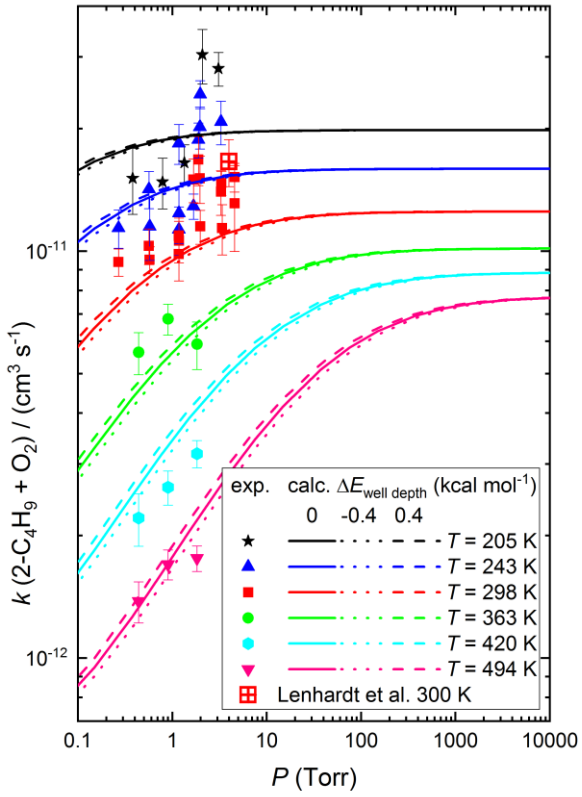

Figure S9. Plot of the experimentally observed (symbols) and theoretically predicted (lines) bimolecular rate coefficients for the 2-butyl + O_2 reaction. The theoretical predictions employ different values for the 2-$C_4H_9O_2$ well depth. The solid lines employ the reference values, while the dotted and dashed lines employ values shifted up and down by 0.4 kcal/mol, respectively.

Finally, in Fig. S10 we explore the sensitivity of the collisionless limit rate coefficients to the barrier heights for both 1-butyl + O_2 and 2-butyl + O_2 reactions. For this parameter, the maximum variation in the predicted bimolecular reaction rate coefficients is about 30%, with the sensitivity gradually increasing with decreasing temperature.

Overall, considering these modest calculated sensitivities, and the good agreement with the experimental data, it seems reasonable to presume that the net 2σ uncertainty in our theoretical predictions is somewhere in the range from a factor of 1.5 to 2.

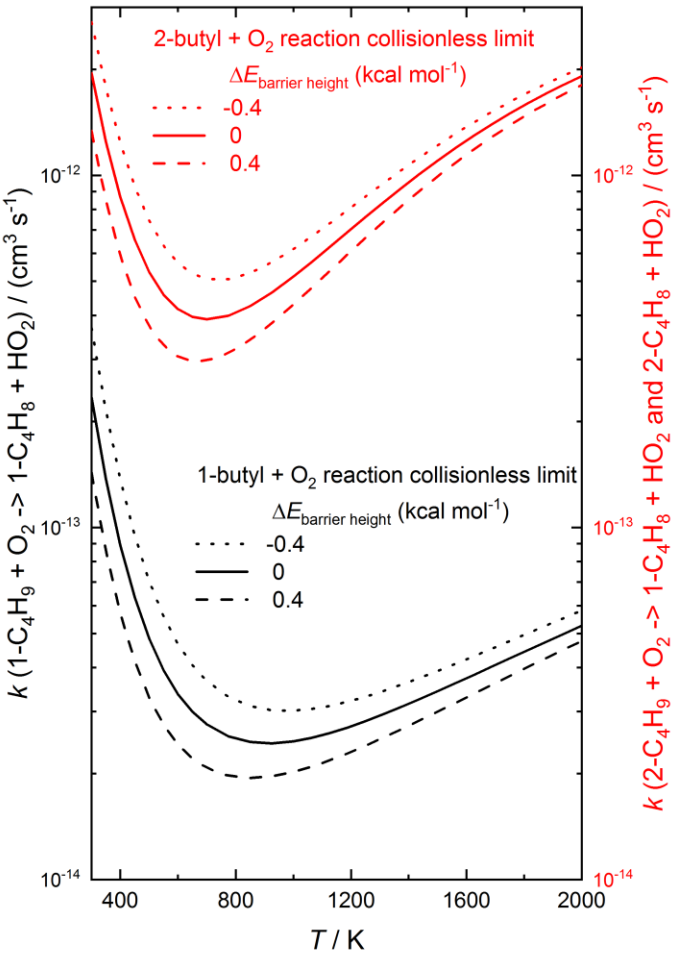

Figure S10. Plot of the theoretically predicted collisionless limit rate coefficients for the 1-butyl + O_2 and 2-butyl + O_2 reactions. The theoretical predictions employ either the reference barrier heights (solid lines) for the transition states producing C_4H_8 + HO_2 or values shifted up (dashed) or down (dotted) by 0.4 kcal/mol.

Supplementary References

[1] J.D. DeSain, C.A. Taatjes, J.A. Miller, S.J. Klippenstein, D.K. Hahn, Faraday Discuss. 119 (2001) 101-120.

[2] G. Ghigo, B.O. Roos, P.A. Malmqvist, Chem. Phys. Lett., 396 (2004) 142-149.